Deep recombination centers in Cu$_2$ZnSnSe$_4$ revealed by screened-exchange hybrid density functional theory

Ye Sheng Yee,[1] Blanka Magyari-Köpe,[1] Yoshio Nishi,[1] Stacey F. Bent,[2] and Bruce M. Clemens[3]

[1]*Department of Electrical Engineering, Stanford University, Stanford, California 94305, USA*
[2]*Department of Chemical Engineering, Stanford University, Stanford, California 94305, USA*
[3]*Department of Materials Science and Engineering, Stanford University, Stanford, California 94305, USA*

We present a comprehensive study of the thermodynamic and electronic properties of intrinsic point defects in the solar energy conversion materials Cu$_2$ZnSnSe$_4$ and CuInSe$_2$ based on the screened-exchange hybrid density functional theory. A comparison between the defect transition levels for Cu$_2$ZnSnSe$_4$ and CuInSe$_2$ reveals that in Cu$_2$ZnSnSe$_4$, the Sn$_{Cu}$ and Sn$_{Zn}$ antisite defects can be recombination centers with defect states close to midgap, while the In$_{Cu}$ antisite defect has a shallow defect level in CuInSe$_2$. The resultant higher Shockley-Read-Hall recombination rate in Cu$_2$ZnSnSe$_4$ reduces the steady-state concentration of minority carriers and quasi-Fermi level separation under illumination. This may explain the origin of the low open-circuit voltage values for Cu$_2$ZnSnSe$_4$ solar cells compared to CuInSe$_2$ solar cells.

I. INTRODUCTION

Cu$_2$ZnSn(S, Se)$_4$ is an emerging and promising solar energy conversion material for high-efficiency, low-cost thin-film solar cells. Unlike conventional thin-film photovoltaic materials like Cu(In, Ga)Se$_2$ and CdTe, the constituents in Cu$_2$ZnSn(S, Se)$_4$ are earth-abundant and nontoxic. Coupled with its suitable band gap (1.0 to 1.5 eV) and relatively high absorption coefficient [1,2], these advantages make Cu$_2$ZnSn(S, Se)$_4$ an ideal candidate material for thin-film photovoltaics. Cu$_2$ZnSn(S, Se)$_4$ solar cells have recently reached a record efficiency of 12.6% [3]. While this is an impressive result, these efficiencies are still significantly lower than the record Cu(In, Ga)Se$_2$ solar cells at around 20% [4]. A comparison between solar cells based on Cu$_2$ZnSn(S, Se)$_4$ and Cu(In, Ga)Se$_2$ reveals similar short-circuit current (J_{sc}) and fill factor (FF) values, but a striking deficit in the open-circuit voltage (V_{oc}) for Cu$_2$ZnSn(S, Se)$_4$.

Several theories have been proposed to explain the V_{oc} limitations in Cu$_2$ZnSn(S, Se)$_4$. These include (i) the existence of tail states due to electrostatic potential fluctuations from charged defects like [Cu$_{Zn}^-$ + Zn$_{Cu}^+$] [5], (ii) absorber-buffer interface recombination dominating over bulk Shockley-Read-Hall recombination in the depletion region [6], (iii) lack of a shallow acceptor leading to carrier freeze-out at low temperatures [7], and (iv) a non-Ohmic back contact at the Mo/Cu$_2$ZnSn(S, Se)$_4$ interface [6]. On the other hand, grain boundaries in high-efficiency Cu$_2$ZnSn(S, Se)$_4$ solar cells have been excluded because scanning Kelvin probe microscopy studies show that they have the same benign characteristics as in Cu(In, Ga)Se$_2$ solar cells and are unlikely to be the limiting factor in Cu$_2$ZnSn(S, Se)$_4$ solar cell efficiencies [8].

It is interesting to note that for Cu$_2$ZnSn(S, Se)$_4$ solar cells, temperature-dependent V_{oc} measurements show an extrapolated V_{oc} value at $T = 0$ K to fall short of the photovoltaic absorber band gap. Indicative of absorber-buffer interface recombination [6], this has been proposed to be a factor limiting V_{oc} in Cu$_2$ZnSn(S, Se)$_4$ solar cells. Nevertheless, the same measurement carried out for the pure selenide semiconductor Cu$_2$ZnSnSe$_4$ yields an extrapolated V_{oc} value

at $T = 0$ K equal to the band gap, demonstrating that the dominant mechanism is Shockley-Read-Hall recombination in the bulk depletion region [9,10]. This mechanism is also a defining characteristic of high-efficiency Cu(In, Ga)Se$_2$ and CdTe solar cells. It is interesting to note that while both Cu$_2$ZnSnSe$_4$ (efficiency = 9.7%) [9] and CuInSe$_2$ solar cells (efficiency = 15%) [11] are limited by Shockley-Read-Hall recombination in the bulk depletion region, and have the same band gaps (1.0 eV) and device structures, they have strikingly different V_{oc} and efficiency values. Under illumination, the separation in the electron and hole quasi-Fermi levels determines the V_{oc}, which is in turn governed by the steady-state concentration of minority carriers and their lifetime. Experimentally, Cu$_2$ZnSnSe$_4$ solar cells were found to have shorter minority carrier lifetimes of 3 ns [12], in contrast with lifetimes of 250 ns in Cu(In, Ga)Se$_2$ solar cells [13]. Thus it is imperative to identify the cause of higher recombination rates in Cu$_2$ZnSnSe$_4$ relative to CuInSe$_2$ in order to shed light on the efficiency differences observed in these materials.

In semiconductors, the presence of native point defects such as vacancies and antisites can lead to intrinsic doping and the formation of defect states within the band gap. Defect states lying close to the conduction or valence bands are considered shallow, and they primarily trap carriers for a short time before thermally reexciting them back to the conduction or valence bands. On the other hand, defect states lying close to the midgap are classified as deep recombination centers, and these states mediate recombination of electron-hole pairs [14]. Such deep recombination centers drastically reduce the concentration of minority carriers and V_{oc} in solar cells.

Both Cu$_2$ZnSnSe$_4$ and CuInSe$_2$ are p-type semiconductors due to their intrinsic point defects, and electrons are the minority carriers. Since the number of holes far exceeds the number of electrons, defect sites need to be electrostatically attractive for the electrons to have a significant interaction with them. Thus donor-type defects that are usually positively-charged and have deep midgap defect states are the most detrimental in Cu$_2$ZnSnSe$_4$ and CuInSe$_2$ solar cells, since they

are attractive to electrons and they increase the recombination rate of electron-hole pairs. Therefore, in this paper, we seek to identify any relevant donor-type defects with deep midgap states. Simulations based on density functional theory (DFT) will be employed to study the characteristics of native point defects and recombination centers in $Cu_2ZnSnSe_4$ and $CuInSe_2$. Chen [15,16] and Nagoya [17] have previously investigated the characteristics of intrinsic point defects in Cu_2ZnSnS_4 using DFT with the GGA functional, where a band gap of only 0.1 eV was reported for Cu_2ZnSnS_4 in Ref. [17]. The study by Persson [18] included the electronic structures and optical properties of defect-free $Cu_2ZnSnSe_4$ and Cu_2ZnSnS_4 crystals using the $GGA + U_d$ method. He showed that the experimental band gaps of both materials can be reproduced if an onsite Coulomb interaction term of $U_d(Cu, Zn) = 4\,eV$ and $U_d(Sn) = 6\,eV$ is included for the d electrons.

Conventionally used exchange-correlation functionals like the local-density approximation (LDA) and generalized-gradient approximation (GGA) are known to significantly underestimate the band gaps of semiconductors, which can lead to large uncertainties in the positions of defect charge state transition levels that lie within the band gap. Although the $GGA + U_d$ method is computationally efficient and partially corrects for the band gap, the choice of the U_d parameter is arbitrary, and may lead to undesired changes in the density of states features, like the valence-band width.

The screened-exchange hybrid density functional proposed by Heyd, Scuseria, and Ernzerhof (HSE06) [19,20] is better-suited for theoretical studies of point defects because it provides an accurate description of the electronic structure and band gaps of semiconductors and insulators [21]. Moreover, the HSE06 functional was shown to give highly accurate charge transition levels for point defects in group-IV semiconductors [22]. In contrast with local and semilocal functionals, HSE06 is also expected to partially correct for the self-interaction errors for localized d electrons [23]. This is especially helpful for copper-containing compounds like $Cu_2ZnSnSe_4$ and $CuInSe_2$. In a previous hybrid DFT study by Paier [24], the HSE06 band structure for Cu_2ZnSnS_4 was validated using G_0W_0 quasiparticle calculations, proving the accuracy of the HSE06 functional. In another study by Han [25], the properties of intrinsic point defects in Cu_2ZnSnS_4 have been reported using the HSE06 functional. Nevertheless, a comprehensive understanding of the intrinsic point defect behavior in $Cu_2ZnSnSe_4$ and $CuInSe_2$ (both materials having the same band gap of 1.0 eV but different electronic behavior) with HSE06 is important to assess the differences in material properties.

In this study, we present a detailed comparison of the intrinsic point defect characteristics between $Cu_2ZnSnSe_4$ and $CuInSe_2$ based on the screened-exchange hybrid density functional HSE06. We have also applied recently-emerged corrections to address the supercell finite-size effects inherent in first-principles calculations [26]. The paper starts with computational details described in Sec. II followed by the results presented in Sec. III, including (A) an evaluation of corrections for supercell finite-size effects, (B) fundamental properties of $Cu_2ZnSnSe_4$ and $CuInSe_2$ crystals, (C) chemical potential stability diagrams, (D) defect formation energies,

(E) charge state transition levels, and (F) defect-induced magnetism. Section IV covers an analysis of the relevant donor-type defects, and Sec. V provides a model to estimate the defect concentrations by self-consistently calculating the Fermi energy (E_F), the concentration of charged defects and concentration of free carriers in $Cu_2ZnSnSe_4$ and $CuInSe_2$.

II. COMPUTATIONAL DETAILS

The screened-exchange hybrid density functional HSE06 as implemented in the Vienna *ab initio* simulation package (VASP) [27] was used in this study. In the HSE06 functional, 25% of the short-range exchange interaction of the Perdew-Burke-Ernzerhof (PBE) [28] generalized-gradient approximation is replaced by the short-range non-local Hartree-Fock (HF) exchange interaction. For this study, an exchange-screening parameter ω of $0.2\,\text{Å}^{-1}$ was applied for both $Cu_2ZnSnSe_4$ and $CuInSe_2$. All calculations were performed using the projector augmented wave (PAW) method [29]. Cu ($3d$, $4s$), In ($4d$, $5s$, $5p$), Zn ($3d$, $4s$), Sn ($4d$, $5s$, $5p$), and Se ($4s$, $4p$) were used as valence electron states. For all calculations of the formation energies and charge transition levels of point defects, $2 \times 2 \times 2$ Γ-centered k-point grids were used for 64-atom supercells. To evaluate the effectiveness of the corrections for supercell finite-size effects, 512-atom supercells with $1 \times 1 \times 1$ Γ-centered k-point grids were used. The perfect defect-free crystal was first fully optimized for the lattice constants and internal ionic coordinates until the residual forces were less than 0.005 eV/Å. These optimized lattice constants were then fixed for supercells containing point defects, and the ions were fully relaxed until residual forces were less than 0.01 eV/Å. Cutoff energies were set to 350 eV for all calculations. The Gaussian smearing method was used to determine the partial occupancies for electrons. In all HSE06 calculations of 64-atom supercells involving point defects in various charge states, spin polarization was enabled. To construct the chemical potential stability diagrams, total energies of secondary phases were also calculated using the same HSE06 hybrid functional.

When performing calculations of point defects involving finite-size supercells with periodic boundary conditions, corrections to the total energies need to be applied to address the artificial electrostatic interactions between charged defects in periodic supercells. We have tested the correction scheme proposed by Freysoldt, Neugebauer, and Van de Walle (FNV) [30], but this scheme cannot be readily applied to defects with large atomic relaxations. Here we choose to apply the Makov-Payne image charge correction scheme [31] because it was found to yield the most reasonable corrections in this study. In this study we have used the Makov-Payne image charge correction to correct the HSE06 total energies for all calculations involving charged defects, using a fraction 0.66 of the monopole correction as proposed in [26]. Theoretical DFT-derived dielectric constants of 8.6 for $Cu_2ZnSnSe_4$ [18] and 8.5 for $CuInSe_2$ [32] were used.

For this study, we focus on cation-related vacancies and antisite defects since high-efficiency $Cu_2ZnSnSe_4$ and $CuInSe_2$ photovoltaic absorbers are typically grown under selenium-rich environments [33]. Selenium vacancies and cation interstitials are thus unlikely to form [34] and were

predicted previously to have higher formation energies than cation vacancies and antisites in Cu$_2$ZnSnSe$_4$ [16]. Therefore they are not included in this study.

The formation energy of a point defect is calculated as

$$\Delta H_f[D, q] = E[D, q] - E_{\text{host}}$$
$$+ \sum n_i \mu_i + q(E_{\text{VBM}} + E_F), \quad (1)$$

where $E[D,q]$ is the total energy of the supercell with a defect D in charge state q, corrected with the Makov-Payne image charge correction scheme that accounts for spurious electrostatic interactions between charged defects in periodic supercells. E_{host} is the total energy of the defect-free supercell. n_i is the number of atoms transferred from the supercell to the chemical reservoir of element i; $n_i = 1$ if an atom is removed and $n_i = -1$ if an atom is added. μ_i refers to the chemical potential of atom i and represents the strength of the chemical reservoir; the formation energy of a vacancy of atom i is high when μ_i is high. E_{VBM} refers to the energy of the valence-band maximum (VBM) and E_F represents the Fermi level, which can vary within the band gap of the material between E_{VBM} and E_{CBM}, where E_{CBM} refers to the energy of the conduction-band minimum (CBM).

The Fermi energy where the charge state of a point defect D changes from q to q' is defined as the charge transition level. Derived from Eq. (1), the following expression can be used to calculate the charge state transition level:

$$\varepsilon[D, q/q'] = (E[D, q] - E[D, q'])/(q' - q) - E_{\text{VBM}}. \quad (2)$$

III. RESULTS AND DISCUSSION

A. Corrections for supercell finite-size effects

Makov and Payne proposed an image charge correction to the total energy of a charged periodic supercell [31]

$$\Delta E_{\text{MP}}(D, q) = \frac{q^2 \alpha_M}{2\varepsilon L} + \frac{2\pi q Q_r}{3\varepsilon L^3}, \quad (3)$$

where α_M is the lattice-dependent Madelung constant, ε is the static dielectric constant, and L is the linear supercell dimension $L = V_{\text{SC}}^{1/3}$. Q_r is the second radial moment of the electron density difference between the defect+host and pure host systems. The first and second terms are the monopole and quadrupole corrections, respectively.

Lany and Zunger later suggested that a scaling of the monopole correction by a constant factor of approximately 0.66 [26] would yield a simple but accurate image charge correction for common supercell geometries:

$$\Delta E_{\text{MP}}(D,q) = (1 + f)\frac{q^2 \alpha_M}{2\varepsilon L}, \quad (4)$$

where $(1 + f) \approx 2/3$. In this study, we have used a fraction 0.66 of the monopole correction for all charged defect calculations.

The performance of the image charge correction scheme was first evaluated by performing test calculations on the Sn$_{\text{Cu}}$ antisite defect for all charge states and the Sn vacancy V$_{\text{Sn}}^{3-}$ and V$_{\text{Sn}}^{4-}$ charge states in Cu$_2$ZnSnSe$_4$ using the PBE functional. Since the image charge correction assumes that the

TABLE I. Uncorrected and image-charge corrected charged defect formation energies ΔH_f for 64-atom supercells and 512-atom supercells. The Fermi energy is set equal to the valence-band maximum ($E_F = 0$) in (1), and the chemical potential μ_i is set equal to its standard state value μ_i^0.

	Uncorrected		Corrected	
Defect	$\Delta H_f(64)$ (eV)	$\Delta H_f(512)$ (eV)	$\Delta H_f(64)$ (eV)	$\Delta H_f(512)$ (eV)
Sn$_{\text{Cu}}^{1+}$ (PBE)	0.70	0.79	0.84	0.86
Sn$_{\text{Cu}}^{2+}$ (PBE)	0.48	0.74	1.02	1.02
Sn$_{\text{Cu}}^{3+}$ (PBE)	0.31	0.73	1.53	1.34
V$_{\text{Sn}}^{3-}$ (PBE)	1.69	2.57	2.91	3.18
V$_{\text{Sn}}^{4-}$ (PBE)	1.61	2.63	3.78	3.71
Sn$_{\text{Cu}}^{1+}$ (HSE06)	0.72		0.86	
Sn$_{\text{Cu}}^{2+}$ (HSE06)	−0.02		0.52	
Sn$_{\text{Cu}}^{3+}$ (HSE06)	−0.76	−0.13	0.47	0.49
V$_{\text{Sn}}^{3-}$ (HSE06)	4.59		5.82	
V$_{\text{Sn}}^{4-}$ (HSE06)	4.92		7.11	

long-range Coulomb interaction is screened by a macroscopic dielectric constant, it is strictly valid only for cubic supercells [35]. Therefore, for this evaluation, we employ supercells containing 64 and 512 atoms since both supercells have approximately cubic dimensions; in both Cu$_2$ZnSnSe$_4$ and CuInSe$_2$, lattice constants $c \approx 2a$. For the 64-atom and 512-atom supercells, $2 \times 2 \times 2$ and $1 \times 1 \times 1$ Γ-centered k-point grids were used, respectively. In order to confirm that the same image charge correction methodology can also be applied to the HSE06 calculations used in this study, we have done calculations for the Sn$_{\text{Cu}}^{3+}$ antisite defect in both 64-atom and 512-atom supercells using the HSE06 functional, in which residual forces were converged to less than 0.01 eV/Å. The potential alignment correction has been shown to be fully included in the image charge correction [35], and is not applied in this study.

Table I shows that the uncorrected formation energies have significant cell size dependencies; errors of $\sim$2.2 eV for the V$_{\text{Sn}}^{4-}$ 64-atom supercell and $\sim$1.1 eV for the V$_{\text{Sn}}^{4-}$ 512-atom supercell exist with the PBE functional. Using the image charge correction, the highest residual errors between the 64-atom and 512-atom supercells with PBE are $\sim$0.2 eV, and the residual error for Sn$_{\text{Cu}}^{3+}$ using HSE06 is 0.02 eV, demonstrating that the image charge correction scheme is applicable for calculations involving both PBE and HSE06 functionals. Since the image charge correction scales as q^2, the Sn$_{\text{Cu}}^{3+}$ antisite defect was selected because of its relatively high charge state; the impact of the correction scheme on the accuracy of the results would be more apparent.

B. Fundamental properties of crystals

Kesterite Cu$_2$ZnSnSe$_4$ with space group $I\bar{4}$ (space group no. 82) belongs to the body-centered tetragonal Bravais lattice. The conventional unit cell has sixteen atoms [Fig. 1(a)]: four Cu atoms on the Wyckoff positions 2a and 2c, two Zn atoms on position 2d, two Sn atoms on position 2b, and eight Se atoms on position 8g. Chalcopyrite CuInSe$_2$ with space group $I\bar{4}2d$
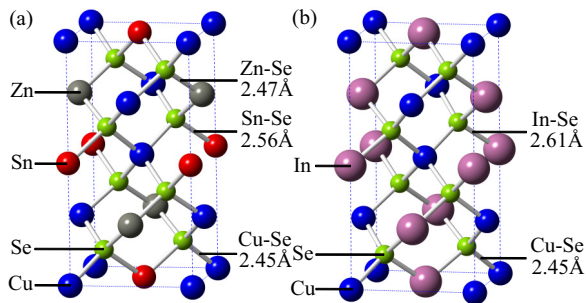
FIG. 1. (Color online) Conventional 16-atom unit cell for (a) kesterite $Cu_2ZnSnSe_4$ and (b) chalcopyrite $CuInSe_2$. The individual bond lengths for both crystals are labeled. Note the similarity in Cu-Se bond lengths for both $Cu_2ZnSnSe_4$ and $CuInSe_2$.

(space group no. 122) is also body-centered tetragonal, and the conventional sixteen-atom unit cell [Fig. 1(b)] contains four Cu atoms on the $4a$ Wyckoff position, four In atoms on the $4b$ position and eight Se atoms on the $8d$ position. Table II summarizes the band gaps and lattice constants calculated using the HSE06 and PBE exchange-correlation functionals, comparing them with experimental values. The calculations indicate that PBE severely underestimates the band gaps for both $Cu_2ZnSnSe_4$ and $CuInSe_2$, and overestimates lattice constants by about 1.5%. The HSE06 calculations show excellent agreement with experimental band gaps and also give better consistency with experimental lattice constants.

The HSE06 band structures for the $Cu_2ZnSnSe_4$ and $CuInSe_2$ primitive unit cells are shown in Fig. 2, plotted along the high symmetry points T $(0, 0, 2\pi/c)$, Γ $(0, 0, 0)$, and N $(\pi/a, \pi/a, 0)$. Spin-orbit coupling has been included in the band structure calculations. The total density of states (DOS) [Fig. 3] was calculated using the tetrahedron method with Blöchl corrections [36]. In both $Cu_2ZnSnSe_4$ and $CuInSe_2$, the upper valence bands are essentially identical, predominantly comprising of the hybridization between the Cu-$3d$ and Se-$4p$ orbitals. The bottom conduction bands are different for the two materials, comprising of interactions between Sn-$5s$ and Se-$4p$ orbitals for $Cu_2ZnSnSe_4$, and In-$5s$ and Se-$4p$ orbitals for $CuInSe_2$. The bottommost conduction band in $Cu_2ZnSnSe_4$ is a lone conduction band separated in energy from other conduction bands, as seen from the band structure in Fig. 2(a). Band structures for both $Cu_2ZnSnSe_4$ and $CuInSe_2$ exhibit direct Γ-point energy gaps. The bands near the valence-band

TABLE II. Band gap E_g, lattice constants a and c, and their ratio c/a for $Cu_2ZnSnSe_4$ and $CuInSe_2$ calculated with the HSE06 and PBE exchange-correlation functionals. Experimental values are also included here for comparison.

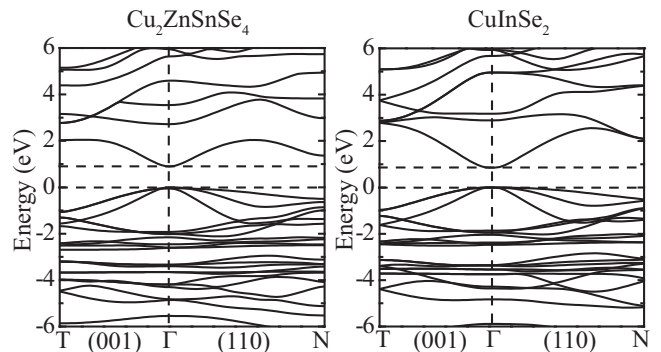|		E_g(eV)	a (Å)	c(Å)	c/a
HSE06	$Cu_2ZnSnSe_4$	0.97	5.73	11.42	1.99
	$CuInSe_2$	0.92	5.82	11.72	2.01
PBE	$Cu_2ZnSnSe_4$	0.03	5.77	11.52	2.00
	$CuInSe_2$	0.01	5.88	11.79	2.01
Expt.	$Cu_2ZnSnSe_4$ [37]	0.98	5.69	11.34	1.99
	$CuInSe_2$ [38,39]	1.02	5.78	11.62	2.01

FIG. 2. Calculated HSE06 band structures for the eight-atom primitive unit cells for (a) $Cu_2ZnSnSe_4$ and (b) $CuInSe_2$. Band structures for both materials are plotted along the high-symmetry directions T-Γ (001) and Γ-N (110). The energy zeros are set to the VBM and the horizontal dashed lines indicate the VBM and CBM.

maximum show relatively flat band dispersions, indicative of larger hole effective masses at those bands. Larger dispersions in the lowest conduction bands in both materials give rise to smaller DOS near the conduction-band minimum (CBM) [Fig. 3].

C. Chemical potential stability diagrams

We can construct chemical potential stability diagrams for $Cu_2ZnSnSe_4$ and $CuInSe_2$ based on the methodology in Refs. [40,41]. From (1), the formation energies of point defects depend on the chemical potentials μ_i of the constituent elements forming the compounds $Cu_2ZnSnSe_4$ and $CuInSe_2$. Defining the relative chemical potential as the chemical
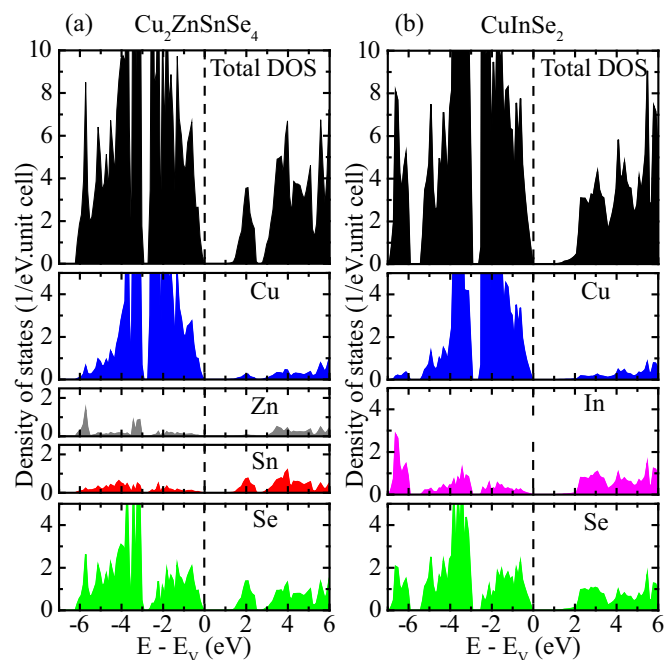

FIG. 3. (Color online) Total and atom-resolved density of states for (a) $Cu_2ZnSnSe_4$ and (b) $CuInSe_2$ calculated with HSE06. The VBM has been referenced to 0 eV in energy.

TABLE III. HSE06 formation energies in eV per formula unit for $Cu_2ZnSnSe_4$, $CuInSe_2$, and their respective secondary phases. The crystal structures and space group symmetries are also given, with the space group number in parenthesis.

	Crystal structure	Space group	ΔH_f
$Cu_2ZnSnSe_4$	Tetragonal	I-4 (82)	−4.36
$CuInSe_2$	Tetragonal	I-42d (122)	−2.40
Cu_2SnSe_3	Monoclinic	Cc (9)	−2.52
$CuSe$	Hexagonal	$P6_3/mmc$ (194)	−0.43
Cu_2Se	Cubic	Fm-3m (225)	−0.63
Cu_3Se_2	Tetragonal	P-42$_1m$ (113)	−1.15
$ZnSe$	Cubic	F-43m (216)	−1.73
$SnSe$	Orthorhombic	$Pnma$ (62)	−0.98
$SnSe_2$	Trigonal	P-3m1 (164)	−1.31
$CuIn_5Se_8$[a]	Tetragonal	I-42d (122)	−8.83
In_2Se_3	Trigonal	$R3m$ (160)	−2.99
$InSe$	Trigonal	$R3m$ (160)	−1.28
In_4Se_3	Orthorhombic	$Pnnm$ (58)	−3.60

[a]Ordered defect compound (ODC) [40].

potential of element i with respect to its standard state ($\Delta\mu_i = \mu_i - \mu_i{}^0$), $\Delta\mu_i$ can take a range of values constrained by the condition that the host compound is stable in thermodynamic equilibrium. Competing secondary phases form outside of this stability range. By calculating the formation energies of the host compounds and all secondary phases, we can construct a chemical potential diagram showing the stability of various phases as a function of the relative chemical potentials of the constituents. The formation energies are calculated at $T = 0$ K and the zero point motion is neglected. Since the chemical potentials of constituent elements are directly controlled by the experimental growth conditions, the defect formation energies and thus defect concentrations can also be controlled.

On the stability diagram, the relative chemical potentials $\Delta\mu_i$ of the constituents are related by the condition that they sum up to the formation energy of the host compound:

$$2\Delta\mu_{Cu} + \Delta\mu_{Zn} + \Delta\mu_{Sn} + 4\Delta\mu_{Se} = \Delta H_f(Cu_2ZnSnSe_4), \quad (5)$$

$$\Delta\mu_{Cu} + \Delta\mu_{In} + 2\Delta\mu_{Se} = \Delta H_f(CuInSe_2). \quad (6)$$

The stable region of the host compound is constrained to the region where secondary phases do not form, i.e., for a secondary phase A_xB_y:

$$x\Delta\mu_A + y\Delta\mu_B \leqslant \Delta H_f(A_xB_y). \quad (7)$$

In addition, the respective elemental solids cannot precipitate, i.e., $\Delta\mu_i \leqslant 0$. The calculated HSE06 chemical potentials $\mu_i{}^0$ for elemental solids Cu (Fm-3m), Zn ($P6_3/mmc$), Sn ($I4_1/amd$), In ($I4/mmm$), and Se ($P3_121$) are −3.07, −1.18, −3.05, −2.32, and −2.38 eV/atom, respectively.

In the calculations of HSE06 formation energies of $Cu_2ZnSnSe_4$, $CuInSe_2$, and their respective competing phases [Table III], the lattice constants and ionic positions were fully relaxed until the residual forces were less than 0.01 eV/Å. The HSE06 exchange-correlation functional is expected to give better agreement for formation energies when compared with the experimental values, especially for copper-containing
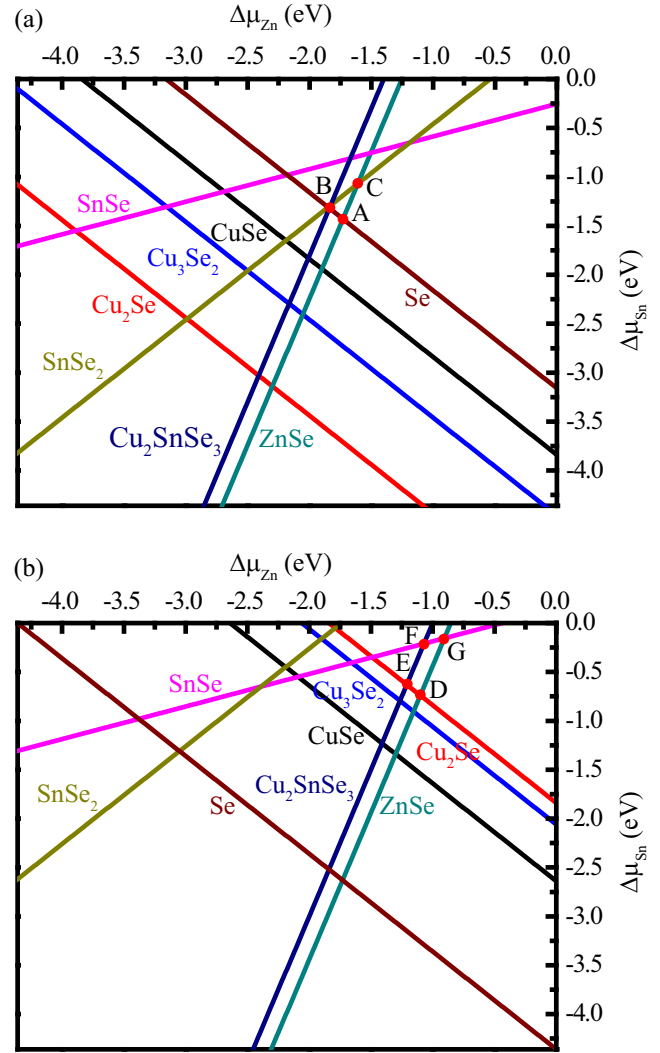

FIG. 4. (Color online) Chemical potential stability diagrams for $Cu_2ZnSnSe_4$ and its secondary phases obtained using HSE06, under (a) copper-poor growth conditions ($\Delta\mu_{Cu} = -0.6$ eV), and (b) copper-rich growth conditions ($\Delta\mu_{Cu} = 0$ eV). In each case, the region in which $Cu_2ZnSnSe_4$ is stable is bound by red dots at the vertices that are labeled A–C in (a) and D–G in (b). The respective secondary phase forms on the side of the line where the phase label lies.

compounds since HSE06 provides an improved description of the localized d electrons in copper [41].

Chemical potential stability diagrams for $Cu_2ZnSnSe_4$ are plotted for both copper-poor conditions ($\Delta\mu_{Cu} = -0.6$ eV) [Fig. 4(a)] and copper-rich conditions ($\Delta\mu_{Cu} = 0$ eV) [Fig. 4(b)]. Below $\Delta\mu_{Cu} = -0.6$ eV, $Cu_2ZnSnSe_4$ is unstable and above $\Delta\mu_{Cu} = 0$ eV, copper metal precipitates. Over the entire range of chemical potential values $\Delta\mu_i$, the stable region for $Cu_2ZnSnSe_4$ is very small, and it is slightly larger under copper-rich conditions than copper-poor conditions. Table IV shows the values $\Delta\mu_i$ of the constituents at the vertices of the stable region for $Cu_2ZnSnSe_4$. Since high-efficiency $Cu_2ZnSnSe_4$ photovoltaic absorbers are generally synthesized under copper-poor, zinc-rich, and selenium-rich growth conditions [42], the relevant vertex to consider is point

TABLE IV. Chemical potentials of the constituent atoms of $Cu_2ZnSnSe_4$ in eV at points A–G in Fig. 4.

	$Cu_2ZnSnSe_4$		
Point	$\Delta\mu_{Cu}$	$\Delta\mu_{Zn}$	$\Delta\mu_{Sn}$
A	−0.60	−1.73	−1.43
B	−0.60	−1.84	−1.32
C	−0.60	−1.61	−1.07
D	0	−1.10	−0.74
E	0	−1.21	−0.63
F	0	−1.07	−0.21
G	0	−0.91	−0.16

TABLE V. Chemical potentials of the constituent atoms of $CuInSe_2$ in eV at points H–L in Fig. 5.

	$CuInSe_2$	
Point	$\Delta\mu_{Cu}$	$\Delta\mu_{In}$
H	−0.79	−1.60
I	−0.46	−0.62
J	0	−0.16
K	0	−1.14
L	−0.43	−1.97

A in Fig. 4(a), which lies along both the Se and ZnSe tie lines under copper-poor growth conditions ($\Delta\mu_{Cu} = -0.6\,eV$). Of particular interest is the stable region for $Cu_2ZnSnSe_4$, which is largely bound by the tie lines for Cu_2SnSe_3 and ZnSe. This finding is consistent with the representation of its cousin Cu_2ZnSnS_4 as a line compound on a pseudobinary phase diagram between Cu_2SnS_3 and ZnS [43]. The most important consequences of this are that (i) small deviations in $\Delta\mu_{Zn}$ easily result in the formation of ZnSe or Cu_2SnSe_3, and (ii) it is more difficult to vary $\Delta\mu_{Zn}$ than $\Delta\mu_{Sn}$ in the formation of stable $Cu_2ZnSnSe_4$.

The chemical potential stability diagram for $CuInSe_2$ is shown in Fig. 5, with the values $\Delta\mu_i$ of the constituents at the vertices of the stable region in Table V. Compared to $Cu_2ZnSnSe_4$, $CuInSe_2$ shows a significantly larger stable region on the phase diagram, manifested as a high tolerance to large off-stoichiometry deviations [40].

It has been shown that high-efficiency $CuInSe_2$ and $Cu(In, Ga)Se_2$ photovoltaic absorbers are prepared under copper-poor and selenium-rich growth conditions [44]. Therefore the relevant vertex to consider is point H in Fig. 5, which
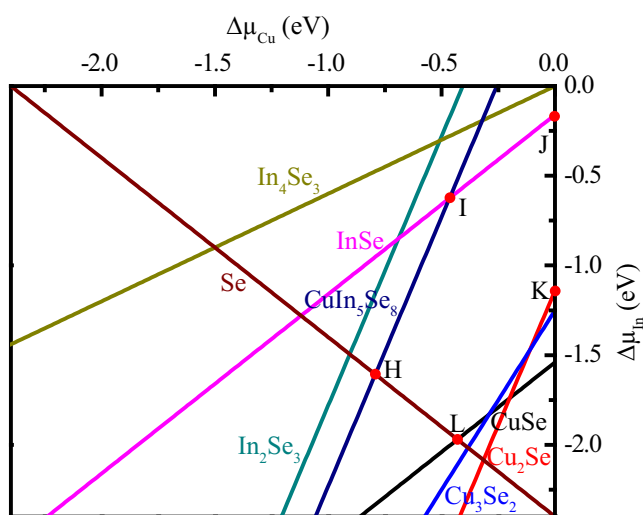
has the lowest $\Delta\mu_{Cu}$ and lies along the Se tie line. Indeed, the presence of 'ordered defect compounds' (ODCs) like $CuIn_5Se_8$ from off-stoichiometry deviations has been reported, in agreement with the point H lying along the $CuIn_5Se_8$ phase boundary.

D. Point defect formation energies

For $Cu_2ZnSnSe_4$, the native point defects included in this study include the cation vacancies (V_{Cu}, V_{Zn}, and V_{Sn}) and cation antisite defects (Cu_{Zn}, Cu_{Sn}, Zn_{Sn}, Zn_{Cu}, Sn_{Cu}, Sn_{Zn}), where X_Y refers to an atom X occupying site Y. These defects are classified as acceptors or donors depending on the valences of the elements. The formal charges for the elements are Cu^{1+}, Zn^{2+}, Sn^{4+}, and Se^{2-} in the $Cu_2ZnSnSe_4$ crystal lattice and thus all cation vacancies are acceptors. Among the antisite defects, Sn_{Cu}, Sn_{Zn}, and Zn_{Cu} are donor-type defects, while the rest are acceptors.

Using (1), the calculated native point defect formation energies ΔH_f at vertex A in Fig. 4(a) (copper-poor, zinc-rich, and selenium-rich conditions) for $Cu_2ZnSnSe_4$ are plotted as a function of Fermi energy in Fig. 6. We have also calculated the equilibrium Fermi level at 300 K (details given in Sec. V) and it is indicated by a vertical dashed line in Fig. 6.

From Fig. 6, we can see that near the equilibrium Fermi level at 300 K (0.27 eV), the point defects with the lowest formation energies (less than 0.5 eV) are Cu_{Zn}, Zn_{Cu}, and V_{Cu}. These are the defects with the highest concentrations in the material and are likely to have the largest impact on bulk electronic properties. This is in agreement with previous *ab initio* studies done using GGA, reporting Cu_{Zn}, Zn_{Cu}, and V_{Cu} as the defects with the lowest formation energies [16]. Experimentally, macroscopically high concentrations (>10%) of site disorder between Cu and Zn have also been observed using neutron powder diffraction [45] and synchrotron radiation x-ray diffraction [46], consistent with the fact that Cu_{Zn} and Zn_{Cu} antisites have the lowest formation energies. At the equilibrium Fermi level of 0.27 eV at 300 K, the charge states of the major point defects are Cu_{Zn}^0 and Cu_{Zn}^{1-}, Zn_{Cu}^{1+}, and V_{Cu}^{1-}, maintaining overall charge neutrality. The other point defects have larger formation energies (higher than 0.5 eV) and are unlikely to dominate the macroscopic electronic properties of $Cu_2ZnSnSe_4$ like its bulk conductivity.

Similarly, Fig. 7 shows the defect formation energies ΔH_f in $CuInSe_2$ as a function of Fermi energy. The equilibrium Fermi level at 300 K (0.15 eV) was calculated with the same procedure described in Sec. V. At the equilibrium Fermi level,
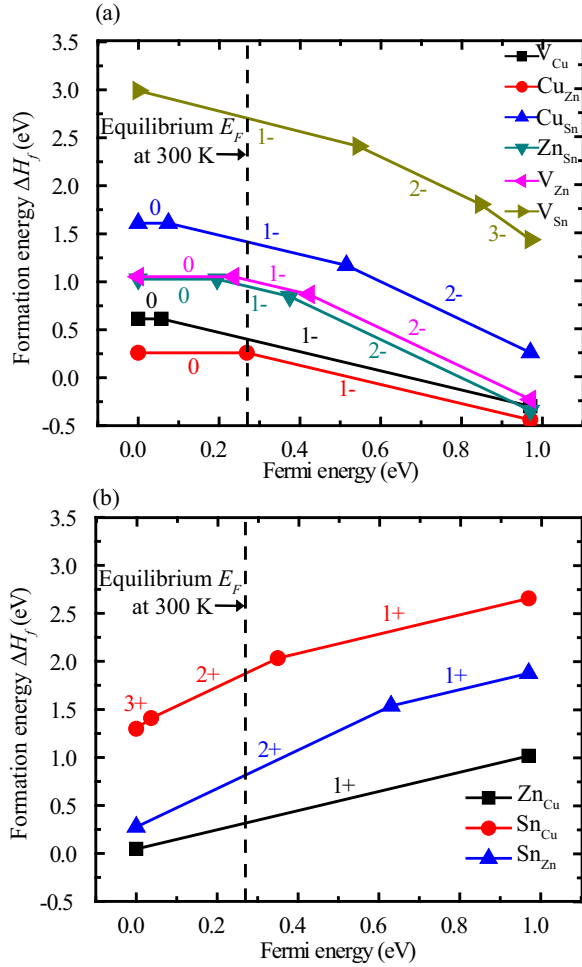

FIG. 5. (Color online) Chemical potential stability diagram for $CuInSe_2$ and its secondary phases obtained using HSE06. The region in which $CuInSe_2$ is stable is bound by red dots at the vertices that are labeled H–L. The respective secondary phase forms on the side of the line where the phase label lies.

(a)

(b)

FIG. 6. (Color online) Defect formation energies for (a) acceptors and (b) donors in $Cu_2ZnSnSe_4$ as a function of Fermi energy at vertex A in Fig. 4(a). The various defect charge states are labeled. The equilibrium Fermi level at 300 K is given by the vertical dashed line.
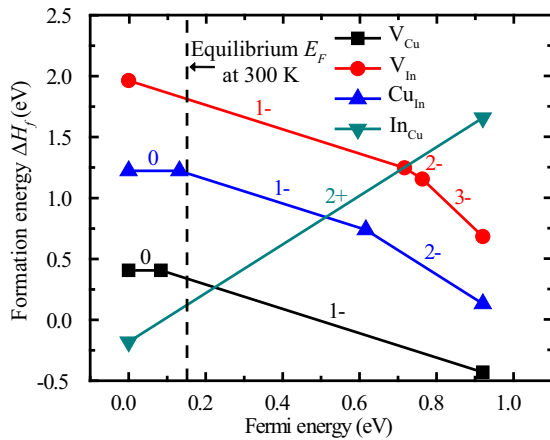

FIG. 7. (Color online) Defect formation energies in $CuInSe_2$ as a function of Fermi energy at vertex H in Fig. 5. The various defect charge states are labeled. The equilibrium Fermi level at 300 K is given by the vertical dashed line.

TABLE VI. Defect formation energies for all charge states in $Cu_2ZnSnSe_4$ and $CuInSe_2$. The Fermi level is set at the VBM, and chemical potentials at their standard state values μ_i^0 ($E_F = 0$, $\Delta\mu_{Cu} = 0$, $\Delta\mu_{Zn} = 0$, $\Delta\mu_{Sn} = 0$, $\Delta\mu_{In} = 0$, and $\Delta\mu_{Se} = 0$).

	+3	+2	+1	0	−1	−2	−3	−4
$Cu_2ZnSnSe_4$								
V_{Cu}				1.21	1.27			
Cu_{Zn}				1.39	1.66			
Cu_{Sn}				2.44	2.52	3.03	4.21	
Zn_{Sn}				0.73	0.92	1.30		
V_{Zn}				2.78	3.02	3.44		
V_{Sn}				4.42	4.39	4.93	5.78	7.11
Zn_{Cu}			−1.08	−0.05				
Sn_{Cu}	0.47	0.50	0.85	2.19				
Sn_{Zn}		0.57	1.20	2.20				
$CuInSe_2$								
V_{Cu}				1.20	1.28			
V_{In}				3.80	3.56	4.28	5.04	
Cu_{In}				2.03	2.17	2.78		
In_{Cu}		−0.99	0.20	1.82				

V_{Cu}^{1-} and In_{Cu}^{2+} are the defects with the lowest formation energies (less than 0.5 eV). These results are qualitatively in agreement with a previous HSE06 study on intrinsic point defects in $CuInSe_2$ [41]. In addition, a previous LDA study also described the ease of forming ($2V_{Cu}^- + In_{Cu}^{2+}$) pairs [40] and its manifestation as ODCs like $CuIn_5Se_8$, $CuIn_3Se_5$, and $Cu_2In_4Se_7$. $CuIn_5Se_8$ is obtained by having a ($2V_{Cu} + In_{Cu}$) pair in every 16-atom conventional unit cell of $CuInSe_2$.

Table VI gives the underlying raw data for the defect formation energies for all relevant charge states. The data are obtained by setting the Fermi energy equal to the VBM and all constituent chemical potentials at their standard state values μ_i^0($E_F = 0$, $\Delta\mu_{Cu} = 0$, $\Delta\mu_{Zn} = 0$, $\Delta\mu_{Sn} = 0$, $\Delta\mu_{In} = 0$, and $\Delta\mu_{Se} = 0$). While these defect formation energies will not occur under physically meaningful growth conditions and Fermi levels, this table is useful for comparison with other values in literature.

E. Charge state transition levels

Generally, point defects can behave either as carrier traps or recombination centers depending on their charge state transition levels. Figure 8 shows the calculated charge state transition levels $\varepsilon[D, q/q']$ using (2) for both $Cu_2ZnSnSe_4$ and $CuInSe_2$. By employing the HSE06 exchange-correlation functional in this study, we find that all relevant charge state transition levels fall within the band gaps of the materials (0.97 eV for $Cu_2ZnSnSe_4$ and 0.92 eV for $CuInSe_2$). A major advantage is the elimination of the need for any postcalculation band gap corrections by rigidly shifting the CBM up relative to the VBM to match the experimental band gap [26,47].

From the perspective of solar cell device physics, positively-charged donor defects have larger capture cross sections for minority carriers (electrons) and play a critical role in electron trapping and recombination. We observe a striking difference in the positions of charge state transition levels for donors in $Cu_2ZnSnSe_4$ and $CuInSe_2$. In $Cu_2ZnSnSe_4$, the
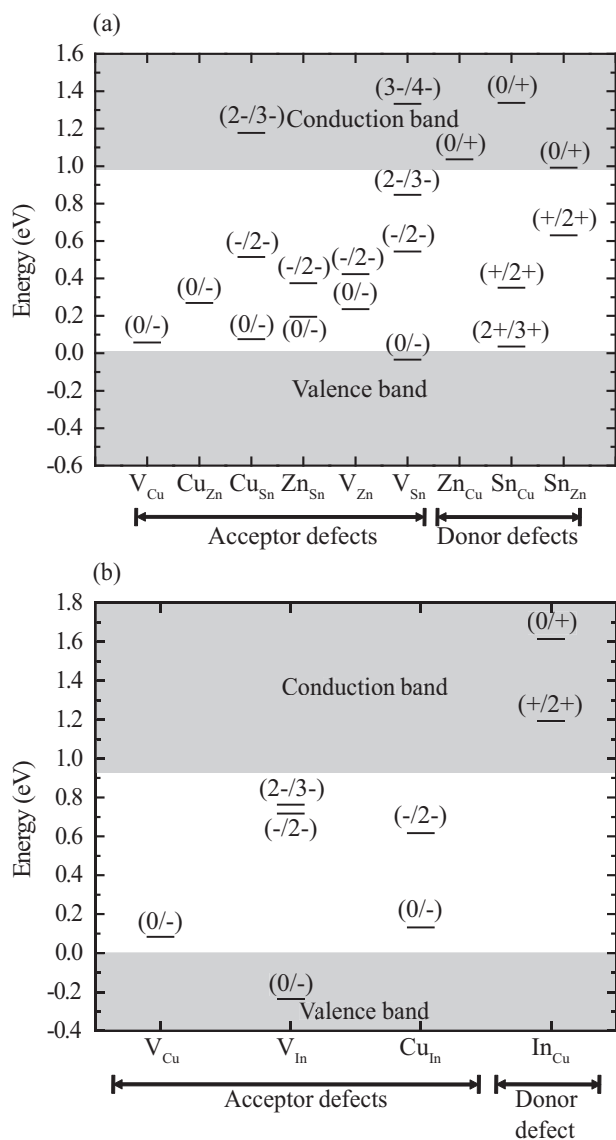
(a)

(b)

FIG. 8. Defect charge state transition levels $\varepsilon[D,q/q']$ for (a) $Cu_2ZnSnSe_4$ and (b) $CuInSe_2$. The same defect transition levels can be visualized in Figs. 6 and 7 as the points connecting the lines representing different charge states.

Sn_{Cu} (+/2+), Sn_{Cu} (2+/3+), and Sn_{Zn} (+/2+) defects yield deep states in the band gap. This is in agreement with a previous HSE06 study by Han [25] on point defects in the pure-sulfide compound Cu_2ZnSnS_4, proposing that the Sn_{Zn} antisite defect has deep midgap states that trap electrons. In particular, the Sn_{Cu} (+/2+) transition level of 0.35 eV lies even below midgap, and very close to the equilibrium Fermi level of 0.27 eV at 300 K. In $CuInSe_2$, however, the relevant In_{Cu} (0/+) and (+/2+) transition levels are both shallow and lie in the conduction band. This concurs with a previous HSE06 study on point defects in $CuInSe_2$, proposing that In_{Cu} is a shallow defect [41]. It is likely that $CuInSe_2$ solar cells can have high efficiencies despite the low formation energy of In_{Cu} because of its shallow defect states. In $Cu_2ZnSnSe_4$, however, the deep midgap Sn_{Cu} and Sn_{Zn} antisite defects increase the Shockley-Read-Hall recombination rate, and the

lower resultant minority carrier concentration can reduce the V_{oc} in $Cu_2ZnSnSe_4$ solar cells. In Sec. IV, we will further analyze the characteristics of Sn_{Cu} and Sn_{Zn} in $Cu_2ZnSnSe_4$, and In_{Cu} in $CuInSe_2$. Zn_{Cu} in $Cu_2ZnSnSe_4$ has a shallow (0/+) transition level and is expected to be an electron trap; captured electrons can be thermally reexcited to the conduction band before recombination can occur.

Among the dominant acceptor defects in $Cu_2ZnSnSe_4$, V_{Cu} has a shallow (0/−) transition level 0.06 eV above the VBM, while Cu_{Zn} has a deeper (0/−) level at 0.27 eV above the VBM, in agreement with Ref. [25]. Having the lowest formation energies of all acceptors, these two defects are expected to have the largest contribution to the p-type conductivity of $Cu_2ZnSnSe_4$. Admittance spectroscopy measurements reveal a dominant acceptor with a transition level 0.13–0.2 eV above the VBM in $Cu_2ZnSn(S, Se)_4$ [7]. This is likely to be the Cu_{Zn} antisite defect considering its lower formation energy and deeper transition level compared to V_{Cu}. The small discrepancy between the calculated transition level of 0.27 eV and the experimentally measured values could be due to (i) inherent uncertainty when accounting for finite supercell-size effects for charged defects or (ii) electrostatic potential fluctuations in the conduction and valence bands due to degenerately high concentrations of Cu_{Zn} and Zn_{Cu}, giving a smaller effective band gap in experiments than predicted. The other acceptor defects in $Cu_2ZnSnSe_4$ have higher formation energies (greater than 1 eV) at the equilibrium Fermi level of 0.27 eV at 300 K and are not expected to influence macroscopic electronic properties. At the equilibrium Fermi level, acceptor defects are unlikely to result in significant minority carrier recombination because these acceptor defects are negatively charged and are repulsive centers to electrons. In $CuInSe_2$, the dominant acceptor defect contributing to p-type conductivity is V_{Cu} given its shallow (0/−) level and its low formation energy, as already shown in previous studies [40,41]. It is interesting to note that the V_{Cu} (0/−) level aligns very well on an absolute scale between $Cu_2ZnSnSe_4$ (0.06 eV) and $CuInSe_2$ (0.08 eV). With similar Cu-Se bond lengths (2.45Å) and Cu-$3d$ and Se-$4p$ antibonding character, the valence-band offset between these two materials can be approximately neglected, giving good alignment between the V_{Cu} (0/−) levels.

F. Defect-induced magnetism

For the Cu_{Sn}^{1-}, Cu_{Sn}^{2-}, Zn_{Sn}^{0}, V_{Zn}^{0}, V_{Sn}^{0}, V_{Sn}^{1-}, V_{Sn}^{2-}, V_{Sn}^{3-}, Sn_{Cu}^{2+}, and Sn_{Zn}^{1+} defects in $Cu_2ZnSnSe_4$ and V_{In}^{0}, V_{In}^{1-}, Cu_{In}^{0}, and Cu_{In}^{1-} defects in $CuInSe_2$, our calculations give a small magnetic moment shown in Fig. 9. All the other defect systems considered in this paper do not show any defect-induced magnetic behavior. An analysis of the density of states for the point defects giving nonzero magnetic moments indicates that the magnetic moments arise from unpaired electrons that are either localized on the point defect for antisites, or on the nearest-neighbor Se atoms for vacancies.

IV. ANALYSIS OF DONOR-TYPE DEFECTS

In Sec. III E, we find that the Sn_{Cu} antisite has deep midgap (+/2+) and (2+/3+) transition levels in $Cu_2ZnSnSe_4$, while in $CuInSe_2$ the In_{Cu} antisite has shallow (0/+) and (+/2+) transition levels lying in the conduction band. The total density

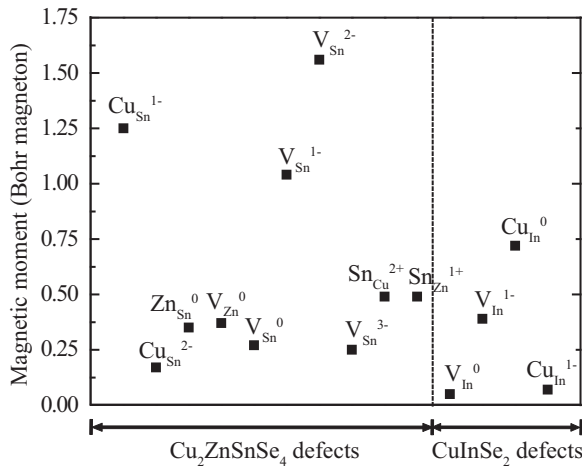FIG. 9. Calculated magnetic moments for point defects in Cu$_2$ZnSnSe$_4$ and CuInSe$_2$.

of states for the Sn$_{Cu}^0$ antisite in Cu$_2$ZnSnSe$_4$ and the In$_{Cu}^0$ antisite in CuInSe$_2$ is plotted in Fig. 10. The deep defect states for Sn$_{Cu}^0$ in Cu$_2$ZnSnSe$_4$ are located within an energy range between 0–0.3 eV above the VBM, while the shallow defect states for In$_{Cu}^0$ in CuInSe$_2$ are located around 0–0.4 eV above the CBM. This observation is in agreement with the

charge transition levels calculated in Fig. 8. Note that for the Sn$_{Cu}^0$ antisite in Cu$_2$ZnSnSe$_4$, Sn donates three extra valence electrons to the supercell when occupying a Cu site. This gives a doubly occupied defect band between 0–0.3 eV above the VBM together with a third electron located in the conduction band, pushing the Fermi level up to ∼1.6 eV. The In$_{Cu}^0$ antisite in CuInSe$_2$ has two extra electrons occupying the same defect band at 0–0.4 eV above the CBM. The total DOS for Sn$_{Zn}$ in Cu$_2$ZnSnSe$_4$ (not shown here) also shows deep defect states like for Sn$_{Cu}$, but the defect states lie closer to midgap between 0.4–0.6 eV above the VBM, in agreement with Fig. 8.

With an extra nuclear charge, Sn is a more electronegative element compared to In. The atomic orbital energies in Sn are lower than in In because electrons in Sn are more tightly bound to the nucleus. Since lower electron orbital energies in Sn result in the formation of deeper states when they interact with the orbitals of the neighboring Se atoms, the Sn$_{Cu}^0$ antisite is expected to give deeper charge transition levels compared to In$_{Cu}^0$ for the same material. To test the validity of this argument, we have also performed HSE06 calculations for a dopant In$_{Cu}^0$ antisite in Cu$_2$ZnSnSe$_4$ and a dopant Sn$_{Cu}^0$ antisite in CuInSe$_2$. The total density of states for these dopant defects are also plotted in Fig. 10. Indeed, the In$_{Cu}^0$ dopant gives shallow defect states in Cu$_2$ZnSnSe$_4$, and the Sn$_{Cu}^0$ dopant gives deep defect states in CuInSe$_2$. Considering the similar sizes of the atoms Sn and In, this
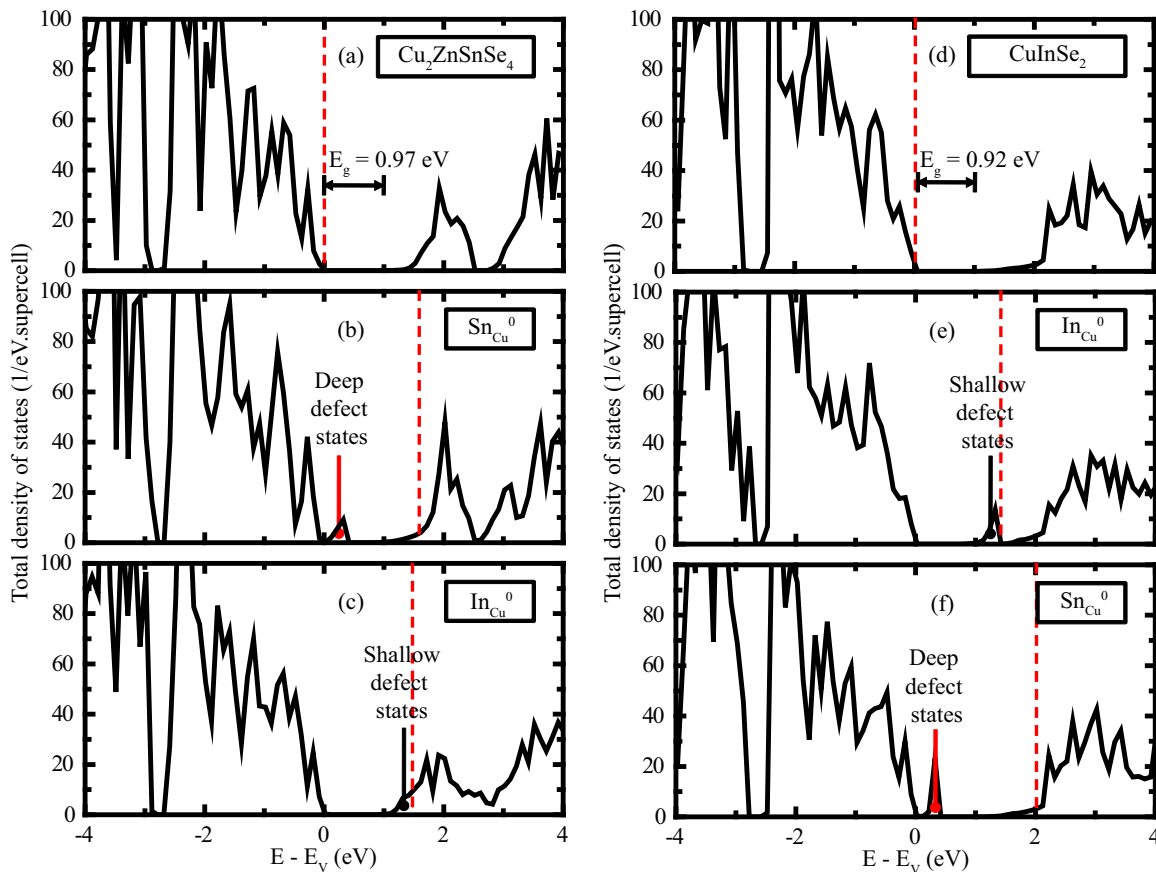

FIG. 10. (Color online) Total density of states for (a) Cu$_2$ZnSnSe$_4$ host crystal, (b) Sn$_{Cu}^0$ antisite in Cu$_2$ZnSnSe$_4$, (c) In$_{Cu}^0$ dopant in Cu$_2$ZnSnSe$_4$, (d) CuInSe$_2$ host crystal, (e) In$_{Cu}^0$ antisite in CuInSe$_2$, and (f) Sn$_{Cu}^0$ dopant in CuInSe$_2$. The VBM has been referenced to 0 eV in energy. Calculated Fermi levels are given by red vertical dashed lines.

TABLE VII. Single-particle defect states within the band gap of $Cu_2ZnSnSe_4$ and $CuInSe_2$ in eV.

	Single-particle defect state
$Cu_2ZnSnSe_4$	
Sn_{Cu}^0	0.31[a]
Sn_{Zn}^0	0.59
Zn_{Cu}^0	PHS[b]
In_{Cu}^0	PHS[b]
$CuInSe_2$	
In_{Cu}^0	1.24[c]
Sn_{Cu}^0	0.30[a]

[a]Deep doubly occupied defect band. The third electron lies in the conduction band and is excluded here.

[b]Perturbed host state.

[c]Shallow doubly occupied defect band lying above the CBM.

indicates the fundamental importance of materials chemistry in determining the positions of defect states—the substitution of In for Zn and Sn can change the underlying defect physics entirely. Neglecting the VBM offset between $Cu_2ZnSnSe_4$ and $CuInSe_2$, we also find that both the Sn_{Cu}^0 and In_{Cu}^0 defect states align very well on an absolute energy scale.

To further enhance the performance of $Cu_2ZnSnSe_4$ solar cells, we propose that a possible solution that can be considered is to intentionally dope $Cu_2ZnSnSe_4$ with indium. If the In_{Cu}^0 dopant defect is preferentially formed in $Cu_2ZnSnSe_4$ relative to the Sn_{Cu}^0 antisite defect, Shockley-Read-Hall recombination can be reduced since shallow defect states are created at the expense of deep midgap states, increasing the steady-state minority carrier concentration under illumination. Indeed, it has been reported that by controlling the diffusion of indium into $Cu_2ZnSn(S, Se)_4$, a V_{oc} enhancement of up to 20% was achieved relative to the control sample without indium, resulting in a solar cell efficiency of 12.7% [48]. While the authors in this study attribute the V_{oc} enhancement in part to an increased carrier density in the $Cu_2ZnSn(S, Se)_4$ absorber, we propose that the V_{oc} enhancement could also be partially attributed to a reduced Shockley-Read-Hall recombination rate giving an increased steady-state minority carrier concentration.

Generally, a deep defect is characterized by the creation of a defect-localized state (DLS) in the band gap. In contrast, a shallow defect has its DLS located inside the host conduction or valence bands. The extra electrons or holes relax from the DLS to the band edge, creating a delocalized perturbed host state (PHS) with essentially the same dispersion as the host bands [26,49]. Recombination via defects is generally expected only when a DLS occurs within the band gap. For the investigated donor defects in $Cu_2ZnSnSe_4$ and $CuInSe_2$, we have tabulated their single-particle defect states in Table VII. Single-particle defect states were calculated by taking the k-point weighted average of the defect state eigenvalues across the entire Brillouin zone (BZ). Since the investigated donor defects are charge-neutral, no image charge corrections are necessary when calculating the single-particle defect states. Lany and Zunger have also shown that for the localized a_1 defect state of the neutral O vacancy V_O in ZnO, single-particle

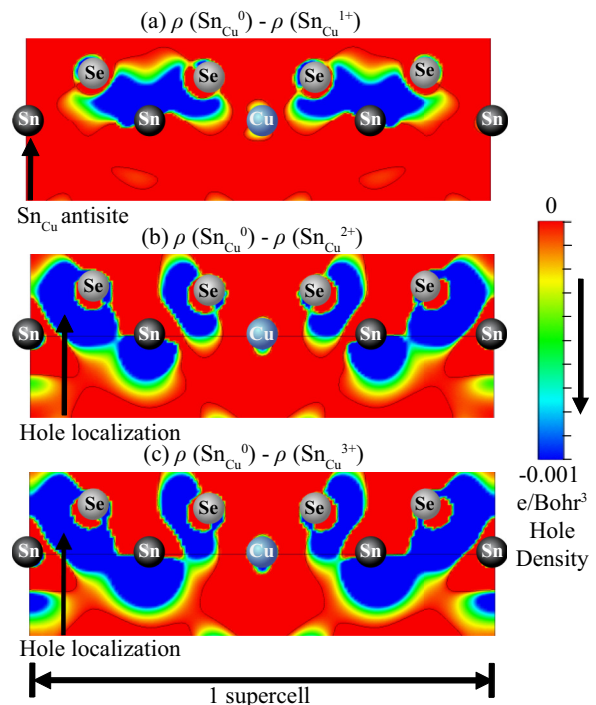FIG. 11. (Color online) Charge density differences ρ along the (1–10) plane for (a) $\rho(Sn_{Cu}^0) - \rho(Sn_{Cu}^{1+})$, (b) $\rho(Sn_{Cu}^0) - \rho(Sn_{Cu}^{2+})$, and (c) $\rho(Sn_{Cu}^0) - \rho(Sn_{Cu}^{3+})$. The red areas correspond to charge-neutral regions and the blue areas correspond to regions with hole densities.

energies have virtually no dependence on supercell size when calculated using a k-point weighted average over the BZ [26], indicating that the single-particle defect states presented in Table VII should be well-converged.

Having established that Sn_{Cu} $(+/2+)$ is a deep transition level at 0.35 eV above the VBM, we now analyze the localization of charge density around the defect, which in turn influences its capture cross section as a recombination center. Figure 11 shows the electron density differences between the various charge states for the Sn_{Cu} antisite along the (1–10) plane. Removing an electron from Sn_{Cu}^0 to form Sn_{Cu}^{1+} [Fig. 11 (a)], we see no localization of holes between the Sn_{Cu} antisite and the nearest Se atoms. However, as we charge the neutral Sn_{Cu}^0 to Sn_{Cu}^{2+} and Sn_{Cu}^{3+}, we observe significant localization of holes on the Sn-Se bond. This implies that despite its 1+ charge state, the Sn_{Cu}^{1+} defect is not repulsive to holes while the Sn_{Cu}^{2+} and Sn_{Cu}^{3+} defects repel holes. Thus, Sn_{Cu} $(+/2+)$ can be an efficient recombination center—after capturing an electron from the conduction band, Sn_{Cu}^{2+} is charged to Sn_{Cu}^{1+} and the Sn_{Cu}^{1+} remains nonrepulsive to a hole from the valence band for recombination. We also observe no change in the Sn-Se bond length when charging Sn_{Cu}^0 to Sn_{Cu}^{1+} (2.82 Å), but charging it to Sn_{Cu}^{2+} induces a relaxation of the Sn-Se bond to 2.70 Å. Further charging the defect to Sn_{Cu}^{3+} relaxes the Sn-Se bond to 2.58 Å. This is consistent with the fact that the excess hole density for Sn_{Cu}^{1+} does not localize around the defect, while the excess charges for Sn_{Cu}^{2+} and Sn_{Cu}^{3+} localize around the defect, giving deep defect-localized states in the band gap.

Doing the same charge localization analysis for Sn_{Zn} in Cu$_2$ZnSnSe$_4$, we observe localization of holes around the defect for both Sn_{Zn}^{1+} and Sn_{Zn}^{2+}, coupled with a relaxation in bond length from 2.81 to 2.68 and 2.58 Å, respectively. With a deep Sn_{Zn} (+/2+) transition level of 0.63 eV above the VBM, significant recombination is expected for the Sn_{Zn} antisite defect, similar to the Sn_{Cu} antisite. The Shockley-Read-Hall recombination rate depends on the defect transition level, defect concentrations, and capture cross sections. While both the Sn_{Cu} and Sn_{Zn} antisite defects exhibit deep midgap transition levels, it is likely that the Sn_{Zn} (+/2+) antisite defect has a smaller capture cross section than the Sn_{Cu} (+/2+) antisite defect because after capturing an electron, the Sn_{Zn}^{1+} state becomes repulsive to a hole from the valence band for recombination, evident from the localization of holes around the Sn_{Zn}^{1+} defect. The exact Shockley-Read-Hall recombination rate, however, would also depend on the respective concentrations of the Sn_{Cu} and Sn_{Zn} defects.

V. DEFECT CONCENTRATIONS

Following the methodology in Refs. [47,50], the equilibrium defect concentrations can be calculated from defect formation energies according to a Boltzmann distribution:

$$C[D,q] = N[D] \exp\left(\frac{-\Delta H_f[D,q]}{k_B T}\right), \qquad (8)$$

where $C[D,q]$ is the concentration of defect D in charge state q, $N[D]$ is the number of possible defect sites, $\Delta H_f[D,q]$ is the formation energy of the defect, k_B is the Boltzmann constant, and T is the absolute temperature used in the growth of Cu$_2$ZnSnSe$_4$ and CuInSe$_2$. Here we use $T = 800$ K. Since the defect concentrations depend on the Fermi energy E_F, which in turn depends on the concentrations of free carriers and charged defects, we determine self-consistently $(E_F, C[D,q]$ and free carrier concentrations) via the charge neutrality condition

$$p - n + \Sigma q C[D,q] = 0, \qquad (9)$$

where p and n are the concentrations of free holes and electrons, respectively. The hole and electron concentrations p and n are calculated from the Fermi-Dirac distribution as

$$p = N_V \frac{1}{1 + [\exp(E_F - E_V)/k_B T]}, \qquad (10)$$

$$n = N_C \frac{1}{1 + [\exp(E_C - E_F)/k_B T]}, \qquad (11)$$

where N_C is the effective electron density of states in the conduction band and N_V is the effective hole density of states in the valence band. N_C and N_V are calculated as

$$N_C = 2\left(\frac{2\pi m_{e,\text{DOS}}^* k_B T}{h^2}\right)^{\frac{3}{2}}, \qquad (12)$$

$$N_V = 2\left(\frac{2\pi m_{h,\text{DOS}}^* k_B T}{h^2}\right)^{\frac{3}{2}}, \qquad (13)$$

where $m_{e,\text{DOS}}^*$ and $m_{h,\text{DOS}}^*$ are the electron and hole effective masses for DOS calculations. For CuInSe$_2$, $m_{e,\text{DOS}}^* = 0.09 m_0$ [51] and $m_{hh}^* = 0.71 m_0$ [52]. Since the experimental value of the hole DOS effective mass $m_{h,\text{DOS}}^*$ is unavailable, we

TABLE VIII. Self-consistently calculated defect concentrations in Cu$_2$ZnSnSe$_4$ at vertex A in Fig. 4(a) at 800 K with E_F at 0.29 eV.

Acceptors	$C[D,q]$ (cm^{-3})	Donors	$C[D,q]$ (cm^{-3})
V_{Cu}^0	1.5×10^{18}	Zn_{Cu}^0	1.6×10^{15}
V_{Cu}^-	4.3×10^{19}	Zn_{Cu}^+	8.2×10^{19}
Cu_{Zn}^0	1.2×10^{20}	Sn_{Cu}^0	1.0×10^3
Cu_{Zn}^-	1.7×10^{20}	Sn_{Cu}^+	4.0×10^9
Cu_{Sn}^0	3.9×10^{11}	Sn_{Cu}^{2+}	9.5×10^9
Cu_{Sn}^-	8.7×10^{12}	Sn_{Cu}^{3+}	2.4×10^8
Cu_{Sn}^{2-}	3.3×10^{11}	Sn_{Zn}^0	6.2×10^9
Cu_{Sn}^{3-}	8.6×10^5	Sn_{Zn}^+	1.6×10^{14}
Zn_{Sn}^0	1.8×10^{15}	Sn_{Zn}^{2+}	2.2×10^{16}
Zn_{Sn}^-	7.2×10^{15}		
Zn_{Sn}^{2-}	2.1×10^{15}		
V_{Zn}^0	1.3×10^{15}		
V_{Zn}^-	2.7×10^{15}		
V_{Zn}^{2-}	3.9×10^{14}		
V_{Sn}^0	8.0×10^2		
V_{Sn}^-	8.7×10^4		
V_{Sn}^{2-}	2.2×10^3		
V_{Sn}^{3-}	6.8×10^{-1}		
V_{Sn}^{4-}	1.8×10^{-7}		

approximate it using m_{hh}^*, giving $N_C = 6.77 \times 10^{17}$ cm^{-3} and $N_V = 1.50 \times 10^{19}$ cm^{-3}. Experimental values for the DOS effective masses are also unavailable for Cu$_2$ZnSnSe$_4$. Since we are interested in an order-of-magnitude estimation of the defect concentrations, we use the electron and hole DOS effective masses $m_{e,\text{DOS}}^*$ and $m_{h,\text{DOS}}^*$ of CuInSe$_2$ for Cu$_2$ZnSnSe$_4$, giving the same values of N_C and N_V. Considering the almost identical valence-band dispersions in both compounds [Figs. 2 and 3], their hole DOS effective masses $m_{h,\text{DOS}}^*$ should be similar. In addition, a theoretical value of $0.08 m_0$ has been reported for m_e^* in Cu$_2$ZnSnSe$_4$ using first-principles calculations [18], very close to the $m_{e,\text{DOS}}^*$ value of $0.09 m_0$ used here. In the calculation of overall charge neutrality, we have used a degeneracy factor of 4 for acceptors and 2 for donors in the Fermi-Dirac distribution function.

The self-consistently calculated defect concentrations at $T = 800$ K for Cu$_2$ZnSnSe$_4$ at vertex A in Fig. 4(a) ($\Delta\mu_{Cu} = -0.6$ eV, $\Delta\mu_{Zn} = -1.73$ eV, and $\Delta\mu_{Sn} = -1.43$ eV) and CuInSe$_2$ at vertex H in Fig. 5 ($\Delta\mu_{Cu} = -0.79$ eV, $\Delta\mu_{In} = -1.60$ eV) are presented in Tables VIII and IX, respectively. The self-consistently calculated E_F values are 0.29 eV for Cu$_2$ZnSnSe$_4$ and 0.25 eV for CuInSe$_2$ at 800 K. If we assume that due to experimental kinetic barriers, the total defect concentrations at 800 K are frozen-in when quenched down to 300 K, we can also calculate the equilibrium Fermi level E_F at 300 K based on the Fermi-Dirac distribution. The calculated E_F value at 300 K for Cu$_2$ZnSnSe$_4$ is 0.27 eV, giving a hole concentration p of 3.8×10^{14} cm^{-3}. For CuInSe$_2$, the calculated E_F value at 300 K is 0.15 eV, with a hole concentration p of 5.5×10^{16} cm^{-3}.

The Shockley-Read-Hall recombination rate depends on the defect concentration, the position of the defect charge

TABLE IX. Self-consistently calculated defect concentrations in CuInSe$_2$ at vertex H in Fig. 5 at 800 K with E_F at 0.25 eV.

Acceptors	$C[D,q]$ (cm^{-3})	Donors	$C[D,q]$ (cm^{-3})
V_{Cu}^0	2.8×10^{19}	In_{Cu}^0	3.0×10^5
V_{Cu}^-	3.0×10^{20}	In_{Cu}^+	1.2×10^{14}
V_{In}^0	1.4×10^8	In_{Cu}^{2+}	1.1×10^{20}
V_{In}^-	1.6×10^{11}		
V_{In}^{2-}	1.7×10^8		
V_{In}^{3-}	9.7×10^4		
Cu_{In}^0	2.0×10^{14}		
Cu_{In}^{1-}	1.1×10^{15}		
Cu_{In}^{2-}	5.0×10^{12}		

transition levels in the band gap, and the capture cross section of the defect. From Table VIII, we see that the defects with charge transition levels deep in the band gap in Cu$_2$ZnSnSe$_4$ [Sn$_{Cu}$ (+/2+) and Sn$_{Zn}$ (+/2+)] have concentrations ranging from 10^{10} to 10^{16} cm^{-3}. Such concentration levels could be significant compared to the steady-state minority carrier concentration ($\sim 10^{12}$ cm^{-3}) in solar cells under standard "1-sun" illumination intensity. While the calculation of defect capture cross sections using first-principles requires further in-depth work beyond the scope of this paper [53], both Sn$_{Cu}$ (+/2+) and Sn$_{Zn}$ (+/2+) are likely to be efficient recombination centers for electrons since these are attractive centers and it is improbable for electrons captured at deep midgap states to be thermally reexcited to the conduction band before recombination. The concomitant higher recombination rate reduces the steady-state minority carrier concentration, explaining the low V_{oc} values observed in Cu$_2$ZnSnSe$_4$ solar cells.

VI. CONCLUSIONS

We have presented a systematic and self-contained study of the intrinsic point defects in Cu$_2$ZnSnSe$_4$ and CuInSe$_2$ using screened-exchange hybrid density functional theory. Among the attractive centers for electrons, the Sn$_{Cu}$ and Sn$_{Zn}$ antisite defects were found to give deep midgap (+/2+) transition levels in Cu$_2$ZnSnSe$_4$. In contrast, In$_{Cu}$ in CuInSe$_2$ was found to be a shallow defect, with transition levels above the CBM. This relative difference in defect transition levels is due to the electronegativity difference between Sn and In. At the growth temperature of 800 K, the defect concentrations of Sn$_{Cu}$ and Sn$_{Zn}$ antisites in Cu$_2$ZnSnSe$_4$ could be significant compared to the steady state minority carrier concentration. This could be a possible explanation for the origin of low V_{oc} values and minority carrier lifetimes in Cu$_2$ZnSnSe$_4$ compared to CuInSe$_2$ solar cells.

[1] J.-S. Seol, S.-Y. Lee, J.-C. Lee, H.-D. Nam, and K.-H. Kim, Sol. Energy Mater. Sol. Cells **75**, 155 (2003).

[2] S. Ozaki and T. Namba, Phys. Status Solidi C **9**, 2403 (2012).

[3] W. Wang, M. T. Winkler, O. Gunawan, T. Gokmen, T. K. Todorov, Y. Zhu, and D. B. Mitzi, Adv. Energy Mater. **4**, 201301465 (2014).

[4] I. Repins, M. A. Contreras, B. Egaas, C. DeHart, J. Scharf, C. L. Perkins, B. To, and R. Noufi, Prog. Photovolt: Res. Appl. **16**, 235 (2008).

[5] T. Gokmen, O. Gunawan, T. K. Todorov, and D. B. Mitzi, Appl. Phys. Lett. **103**, 103506 (2013).

[6] O. Gunawan, T. K. Todorov, and D. B. Mitzi, Appl. Phys. Lett. **97**, 233506 (2010).

[7] O. Gunawan, T. Gokmen, C. W. Warren, J. D. Cohen, T. K. Todorov, D. A. R. Barkhouse, S. Bag, J. Tang, B. Shin, and D. B. Mitzi, Appl. Phys. Lett. **100**, 253905 (2012).

[8] J. B. Li, V. Chawla, and B. M. Clemens, Adv. Mater. **24**, 720 (2012).

[9] G. Brammertz, M. Buffière, S. Oueslati, H. ElAnzeery, K. B. Messaoud, S. Sahayaraj, C. Köble, M. Meuris, and J. Poortmans, Appl. Phys. Lett. **103**, 163904 (2013).

[10] A. Redinger, M. Mousel, R. Djemour, L. Gütay, N. Valle, and S. Siebentritt, Prog. Photovolt: Res. Appl. **22**, 51 (2014).

[11] L. Stolt, J. Hedström, J. Kessler, M. Ruckh, K. O. Velthaus, and H. W. Schock, Appl. Phys. Lett. **62**, 597 (1993).

[12] I. L. Repins, H. Moutinho, S. G. Choi, A. Kanevce, D. Kuciauskas, P. Dippo, C. L. Beall, J. Carapella, C. DeHart, B. Huang, and S. H. Wei, J. Appl. Phys. **114**, 084507 (2013).

[13] W. K. Metzger, I. L. Repins, and M. A. Contreras, Appl. Phys. Lett. **93**, 022110 (2008).

[14] J.W. Mayer, and S.S. Lau, *Electronic Materials Science: For Integrated Circuits in Si and GaAs* (Macmillan Publishing, New York, 1990), p. 160.

[15] S. Chen, A. Walsh, X. G. Gong, and S.-H. Wei, Adv. Mater. **25**, 1522 (2013).

[16] S. Chen, J.-H. Yang, X. G. Gong, A. Walsh, and S.-H. Wei, Phys. Rev. B **81**, 245204 (2010).

[17] A. Nagoya, R. Asahi, R. Wahl and G. Kresse, Phys. Rev. B **81**, 113202 (2010).

[18] C. Persson, J. Appl. Phys. **107**, 053710 (2010).

[19] J. Heyd, G. E. Scuseria, and M. Ernzerhof, J. Chem. Phys. **118**, 8207 (2003).

[20] J. Heyd, G. E. Scuseria, and M. Ernzerhof, J. Chem. Phys. **124**, 219906 (2006).

[21] T. M. Henderson, J. Paier, and G. E. Scuseria, *Advanced Calculations for Defects in Materials* (Wiley-VCH, Weinheim, 2011), p. 97.

[22] P. Deák, B. Aradi, T. Frauenheim, E. Janzén, and A. Gali, Phys. Rev. B **81**, 153203 (2010).

[23] A. Stroppa, G.Kresse, and A. Continenza, Phys. Rev. B **83**, 085201 (2011).

[24] J. Paier, R. Asahi, A. Nagoya, and G. Kresse, Phys. Rev. B **79**, 115126 (2009).

[25] D. Han, Y. Y. Sun, J. Bang, Y. Y. Zhang, H.-B. Sun, X.-B. Li, and S. B. Zhang, Phys. Rev. B **87**, 155206 (2013).

[26] S. Lany and A. Zunger, Phys. Rev. B **78**, 235104 (2008).

[27] G. Kresse and J. Furthmüller, Phys. Rev. B **54**, 11169 (1996).

[28] J. P. Perdew, K. Burke, and M. Ernzerhof, Phys. Rev. Lett. **77**, 3865 (1996).

[29] P. E. Blöchl, Phys. Rev. B **50**, 17953 (1994).

[30] C. Freysoldt, J. Neugebauer, and C. G. Van de Walle, Phys. Rev. Lett. **102**, 016402 (2009).

[31] G. Makov and M. C. Payne, Phys. Rev. B **51**, 4014 (1995).

[32] A. Soni, A. Dashora, V. Gupta, C. M. Arora, M. Rérat, B. L. Ahuja, and R. Pandey, J. Electron. Mater. **40**, 2197 (2011).

[33] G. Hanna, J. Mattheis, V. Laptev, Y. Yamamoto, U. Rau, and H. W. Schock, Thin Solid Films **431**, 31 (2003).

[34] D. Mutter and S. T. Dunham, *Fortieth IEEE Photovoltaic Specialists Conference, June 2014, Denver, CO, USA* (IEEE, Piscataway, 2014), p. 2384.

[35] Y. Kumagai and F. Oba, Phys. Rev. B **89**, 195205 (2014).

[36] P. E. Blöchl, O. Jepsen, and O. K. Andersen, Phys. Rev. B **49**, 16223 (1994).

[37] F. Gao, S. Yamazoe, T. Maeda, and T. Wada, Jpn. J. Appl. Phys. **51**, 10NC28 (2012).

[38] D. K. Suri, K. C. Nagpal, and G. K. Chadha, J. Appl. Cyst. **22**, 578 (1989).

[39] H. Neumann, Solar Cells **16**, 317 (1986).

[40] S. B. Zhang, S.-H. Wei, A. Zunger, and H. Katayama-Yoshida, Phys. Rev. B **57**, 9642 (1998).

[41] J. Pohl and K. Albe, Phys. Rev. B **87**, 245203 (2013).

[42] H. Katagiri, K. Jimbo, M. Tahara, H. Araki, and K. Oishi, Mater. Res. Soc. Symp. Proc. **1165**, M04 (2009).

[43] I.D. Olekseyuk, I.V. Dudchak, L.V. Piskach, J. Alloys Compd. **368**, 135 (2004).

[44] M. A. Contreras, B. Egaas, K. Ramanathan, J. Hiltner, A. Swartzlander, F. Hasoon, and R. Noufi, Prog. Photovolt: Res. Appl. **7**, 311 (1999).

[45] S. Schorr, Sol. Energy Mater. Sol. Cells **95**, 1482 (2011).

[46] T. Washio, H. Nozaki, T. Fukano, T. Motohiro, K. Jimbo, and H. Katagiri, J. Appl. Phys. **110**, 074511 (2011).

[47] C. Persson, Y.-J. Zhao, S. Lany, and A. Zunger, Phys. Rev. B **72**, 035211 (2005).

[48] J. Kim, H. Hiroi, T. K. Todorov, O. Gunawan, M. Kuwahara, T. Gokmen, D. Nair, M. Hopstaken, B. Shin, Y. S. Lee, W. Wang, H. Sugimoto, D. B. Mitzi, Adv. Mater. **26**, 7427 (2014).

[49] C. Freysoldt, B. Grabowski, T. Hickel, J. Neugebauer, G. Kresse, A. Janotti, and C. G. Van de Walle, Rev. Mod. Phys. **86**, 253 (2014).

[50] Y. Kumagai, M. Choi, Y. Nose, and F. Oba, Phys. Rev. B **90**, 125202 (2014).

[51] H. Weinert, H. Neumann, H.-J. Höbler, G. Kühn, and N.-V. Nam, Phys. Status Solidi B **81**, K59 (1977).

[52] H. Neumann, H. Sobotta, W. Kissinger, V. Riede, and G. Kühn, Phys. Status Solidi B **108**, 483 (1981).

[53] A. Alkauskas, Q. Yan, and C. G. Van de Walle, Phys. Rev. B **90**, 075202 (2014).

[54] K. Momma and F. Izumi, J. Appl. Crystallogr. **41**, 653 (2008).